

HI scale height in dwarf galaxies

Narendra Nath Patra¹ *

¹ Raman Research Institute, C. V. Raman Avenue, Sadashivanagar, Bengaluru 560080, India

ABSTRACT

Assuming a vertical hydrostatic equilibrium in the baryonic discs, joint Poisson’s-Boltzmann equation was set up and solved numerically in a sample of 23 nearby dwarf galaxies from the LITTLE-THINGS survey. This is the largest sample to date for which detailed hydrostatic modeling is performed. The solutions of the Poisson’s-Boltzmann equation provide a complete three-dimensional distribution of the atomic hydrogen (HI) in these galaxies. Using these solutions, we estimate the vertical scale height (defined as the Half Width at Half Maxima (HWHM) of the density distribution) of the HI as a function of radius. We find that the scale height in our sample galaxies varies between a few hundred parsecs at the center to a few kiloparsecs at the edge. These values are significantly higher than what is observed in spiral galaxies. We further estimate the axial ratios to investigate the thickness of the HI discs in dwarf galaxies. For our sample galaxies, we find a median axial ratio to be 0.40, which is much higher than the same observed in the Milky Way. This indicates that the vertical hydrostatic equilibrium results in thicker HI discs in dwarf galaxies naturally.

Key words: radio lines: ISM – atomic data – galaxies: structure – galaxies: kinematics and dynamics – galaxies: dwarfs

1 INTRODUCTION

The local volume dwarf galaxies can be regarded as the analogs of the galaxies in the early universe. According to the hierarchical model of structure formation, the smaller galaxies form first, and then they merge to form larger galaxies. In that sense, local volume dwarf galaxies can be considered to be representative of the building blocks of the early universe. Not only that, the star formation rate and metallicities observed in these galaxies are very similar to what is expected in the Inter-Stellar Medium (ISM) of the early galaxies (Hunter 2008; Ekta, Chengalur & Pustilnik 2008; Bigiel et al. 2010). Hence, it is essential to investigate the structure and the distribution of the ISM in these galaxies. Especially, the atomic hydrogen (HI) component, which dominates the ISM at every radius in these galaxies (Hunter et al. 2012; Schruba et al. 2012).

The HI in dwarf galaxies acts as the fuel reservoir for star formation and can significantly influence the evolution of such galaxies. Though, stars form out of molecular clouds, no significant molecular gas has been detected in these galaxies despite substantial efforts (see, e.g., Taylor, Kobulnicky & Skillman 1998; Schruba et al. 2012). Moreover, the HI in these galaxies found to follow the well known Kennicutt-Schmidt law (Kennicutt 1998; Bigiel et al. 2010; Roychowdhury et al. 2009, 2011, 2014; Patra et al. 2016a; Roychowdhury, Chengalur & Shi 2017), indicating a direct connection between the HI surface density and the star formation rate density. However, despite its tremendous importance, the three-dimensional distribu-

tion of the HI and its implications to the structure, shape, star formation, etc. are not well understood to date. For instance, the volume density of the HI and the mid-plane pressure could help in understanding the star formation in connection to its instability criteria (Toomre 1964; Goldreich & Lynden-Bell 1965). Not only that, but it can also provide crucial inputs to the development of the theoretical frameworks for star formation processes in the ISM and origin of the star formation laws (Wolfire et al. 1995; Dekel et al. 2019).

For example, Bacchini et al. (2019a) (see also, Bacchini et al. (2019b)) employed the hydrostatic equilibrium condition in a sample of 12 nearby disc galaxies to calculate the volume densities of the gas (atomic and molecular) and the star formation rates to derive a Volumetric Star Formation (VSF) law. They found that their VSF shows much less scatter than what is observed in the traditional Kennicutt-Schmidt law (Kennicutt 1998) determined using surface densities. This indicates that the volume densities of different ISM phases might be more fundamental (and hence the VSF) to star formation processes than the surface densities.

Not only that, but the distribution of gas in the vertical direction has many other implications too. For example, the thickness of the HI discs in dwarf galaxies (which are analogs to the galaxies in the early universe) mainly decides the absorption cross-section to the background quasars, which in turn determines the average number of absorbers expected per unit redshift (see, e.g. Zwaan et al. 2005; Patra, Chengalur & Begum 2013). This could be crucial in understanding the origin of the high-redshift Damped Lyman α systems (see, e.g., Wolfe et al. 1986; Prochaska & Wolfe 1997; Haehnelt, Steinmetz & Rauch

* E-mail: narendra@rri.res.in

1998). The thickness of the HI discs further decides the sizes of the bubbles/super-bubbles up to which it can grow before breaking out into the Inter-Galactic Medium (IGM). In that sense, it controls the mixing of the high metallicity gas into the IGM. Moreover, the intrinsic shape of the galaxies is a fundamental parameter that must be produced by the galaxy evolutionary models to be consistent with the observations.

Hence, in these respects, it is imperative to estimate the distribution of the HI and, subsequently, the scale heights (defined as Half-Width at Half Maxima) in galaxies. However, measuring the HI distribution directly from observation is not straight forward. Even for the Milky Way, having to reside within it, rigorous modeling is required to estimate the three-dimensional distribution of the HI from the observed brightness temperature profiles (see, e.g., Kalberla et al. 2007; Kalberla & Dedes 2008). For external galaxies, on the other hand, the lack of spatial resolution and the line-of-sight projection effects make it more challenging to estimate the volume densities using direct measurements. Only for special cases, e.g., for a constant scale height as a function of radius observed in an edge-on orientation, allows one to measure the scale height directly. However, for real galaxies, the scale height is never found to be constant, and hence, effectively, in all cases, detailed modeling assisted by observation is needed (see, e.g., Narayan & Jog 2002a,b; Banerjee & Jog 2007; Patra et al. 2014).

In this work, we model the discs of dwarf galaxies as a two-component system consists of stars and HI in hydrostatic equilibrium under their mutual gravity in the external force field of the dark matter halo. Under this assumption, we set up the joint Poisson's-Boltzmann equation of hydrostatic equilibrium and numerically solve it. The solution of the Poisson's-Boltzmann equation provides the density of the gas and stars as a function of the height from the mid-plane (z) at different radii. This, in turn, provides a detailed three-dimensional distribution of the HI in a galaxy. A number of previous studies used similar modeling techniques to estimate the gas/stellar distribution in galaxies theoretically. For example, in early studies, Narayan & Jog (2002b) solved the Poisson's-Boltzmann equation for a three-component disc in a self-consistent manner. Later, several other studies used this method to estimate the HI/molecular scale heights in spiral galaxies (Banerjee & Jog 2007, 2008; Banerjee, Matthews & Jog 2010; Patra 2018, 2019). Banerjee et al. (2011a) used this technique to solve the hydrostatic equilibrium equation in four dwarf galaxies. They found that the HI scale height in dwarf galaxies are larger than what is found in spiral galaxies. In this paper, we solve the joint Poisson's-Boltzmann equation of hydrostatic equilibrium self-consistently in a sample of 23 galaxies from the Local Irregulars That Trace Luminosity Extremes - The HI Nearby Galaxy Survey (LITTLE-THINGS) (Hunter et al. 2012). This is the largest sample to date for which a theoretical determination of the three-dimensional density distribution of the HI is attempted.

2 SAMPLE

We choose our sample galaxies from the LITTLE-THINGS survey for which all the necessary data are available publicly. The LITTLE-THINGS sample consists of 41 galaxies, which are observed in HI using the Very Large Array (VLA). Out of these 41 galaxies, 37 are classified as dwarf irregulars, whereas four galaxies are classified as Blue Compact Dwarfs (BCDs). As we will see in the next section, the rotation curve of a galaxy plays a crucial input to the hydrostatic equation. Hence, it is necessary to have the rotation curve measured for a galaxy to consider it for hydrostatic modeling. Unfortunately, out of 41 sam-

ple galaxies in the LITTLE-THINGS survey, the rotation curve could be extracted only for 26 galaxies (see Oh et al. 2015, for more details). Moreover, to avoid any divergence while solving the Poisson's-Boltzmann equation, we needed to fit the rotation curves of our sample galaxies with a smooth function (see §3.1 for more details). Traditionally, a Brandt profile (Brandt 1960) is used to represent a typical rotation curve. For three galaxies, i.e., DDO 46, F564-V3, and IC 1613, the rotation curves could not be well represented by a Brandt profile (or a more simpler straight line) due to their sharply declining nature at outer radii. We exclude these three galaxies from our final sample. This leads to a total of 23 dwarf irregular galaxies for which we set up the Poisson's-Boltzmann equation and solve numerically to obtain the three-dimensional distribution of the HI in them. In table 2 we present the basic properties of our sample galaxies. As can be seen from the table, our sample galaxies trace the low mass end of the HI mass function having HI masses $< 10^9 M_{\odot}$. These low mass galaxies are particularly interesting due to their similarities to the galaxies expected in the early universe.

3 MODELLING THE GALAXY DISCS

We consider the galactic discs in dwarf galaxies to be a two-component system consisting of an HI and a stellar disc. We note that no considerable amount of molecular gas has been detected in dwarf galaxies despite several significant efforts (Taylor, Kobulnicky & Skillman 1998; Schruha et al. 2012). Hence, we ignore the contribution of the molecular gas in the formulation of the hydrostatic equation. Unlike spiral galaxies where the stellar discs dominate the gravity within the optical radii, in dwarf galaxies, the HI contributes to the disc surface density equally or more as compared to the stellar disc (over all radii). In other words, the gas discs in dwarf galaxies are more critical in deciding the hydrostatic equilibrium than the stellar discs.

We assume that the stellar and the gas discs in dwarf galaxies are in vertical hydrostatic equilibrium under the total gravity of the baryonic discs (star+HI) and the dark matter halo, balanced by the vertical pressure generated by the velocity dispersions of the individual components. To simplify the modeling, we further assume that both the baryonic discs are co-planar and concentric with the centers coinciding with the center of the dark matter halo. Under these assumptions, one then can write the Poisson's equation of hydrostatic equilibrium in cylindrical coordinate as

$$\frac{1}{R} \frac{\partial}{\partial R} \left(R \frac{\partial \Phi_{tot}}{\partial R} \right) + \frac{\partial^2 \Phi_{tot}}{\partial z^2} = 4\pi G \left(\sum_{i=1}^2 \rho_i + \rho_h \right) \quad (1)$$

where Φ_{tot} is the total gravitational potential due to the baryonic discs and the dark matter halo. Whereas, ρ_i denotes the volume density of the two disc components (stars and HI). ρ_h represents the volume density of the underlying dark matter halo, which is an input parameter to our modeling and estimated by the mass-modeling of the rotation curve.

In Eq. 1, Φ_{tot} is not a directly measurable quantity. Instead, it relates to the pressure gradient as a requirement of the static equilibrium

$$\frac{\partial}{\partial z} (\rho_i \langle \sigma_z^2 \rangle_i) + \rho_i \frac{\partial \Phi_{tot}}{\partial z} = 0 \quad (2)$$

i.e., in static equilibrium, the gradient of the potential would be balanced by the gradient in pressure.

Using Eq. 2, we can rewrite Eq. 1 as

Name	RA (J2000) (h m s)	DEC (J2000) (° ' ")	Dist (Mpc)	M _V (mag)	R _H (')	R _D (kpc)	log M _{HI} (M _⊙)	i (°)
(1)	(2)	(3)	(4)	(5)	(6)	(7)	(8)	(9)
CVnIrwA	12 38 39.2	+32 45 41.0	3.6	-12.4	0.87	0.41	7.67	66.5
DDO 101	11 55 39.1	+31 31 9.9	6.4	-15.0	1.05	0.94	7.36	51.0
DDO 126	12 27 06.6	+37 08 15.9	4.9	-14.9	1.76	0.87	8.16	65.0
DDO 133	12 32 55.2	+31 32 19.1	3.5	-14.8	2.33	1.24	8.02	43.4
DDO 154	12 54 05.7	+27 09 09.9	3.7	-14.2	1.55	0.59	8.46	68.2
DDO 168	13 14 27.3	+45 55 37.3	4.3	-15.7	2.32	0.82	8.47	46.5
DDO 210	20 46 51.6	-12 50 57.7	0.9	-10.9	1.31	0.17	6.30	66.7
DDO 216	23 28 34.7	+14 44 56.2	1.1	-13.7	4.00	0.54	6.75	63.7
DDO 43	07 28 17.7	+40 46 08.3	7.8	-15.1	0.89	0.41	8.23	40.6
DDO 47	07 41 55.3	+16 48 07.1	5.2	-15.5	2.24	1.37	8.59	45.5
DDO 50	08 19 03.7	+70 43 24.6	3.4	-16.6	3.97	1.10	8.85	49.7
DDO 52	08 28 28.4	+41 51 26.5	10.3	-15.4	1.08	1.30	8.43	43.0
DDO 53	08 34 06.4	+66 10 47.9	3.6	-13.8	1.37	0.72	7.72	27.0
DDO 70	10 00 00.9	+05 20 12.9	1.3	-14.1	3.71	0.48	7.61	50.0
DDO 87	10 49 34.9	+65 31 47.9	7.7	-15.0	1.15	1.31	8.39	55.5
Haro 29	12 26 18.4	+48 29 40.4	5.9	-14.6	0.84	0.29	7.80	61.2
Haro 36	12 46 56.6	+51 36 47.3	9.3	-15.9	-	0.69	8.16	70.0
IC 10	00 20 18.9	+59 17 49.9	0.7	-16.3	-	0.40	7.78	47.0
NGC 1569	04 30 46.2	+64 51 10.3	3.4	-18.2	-	0.38	8.39	69.1
NGC 2366	07 28 53.4	+69 12 49.6	3.4	-16.8	4.72	1.36	8.84	63.0
NGC 3738	11 35 46.9	+54 31 44.8	4.9	-17.1	2.40	0.78	8.06	22.6
UGC 8508	13 30 44.9	+54 54 32.4	2.6	-13.6	1.28	0.27	7.28	82.5
WLM	00 01 59.9	-15 27 57.2	1.0	-14.4	5.81	0.57	7.85	74.0

Table 1. Basic properties of our sample galaxies. The first column shows the name of the galaxies. Column (2) and (3) represent the RA and DEC coordinates, whereas column (4) denotes the distances to the galaxies. Column (5) shows the absolute V band magnitude. In column (6) and (7), we quote the Holmberg radius and the disc scale length in the optical band, respectively. Column (8) and (9) show the HI mass and the inclination of the HI discs, respectively. All the data in column (4) to (8) are obtained from Walter et al. (2008), whereas data in column (9) is taken from Oh et al. (2015).

$$\begin{aligned}
 \langle \sigma_z^2 \rangle_i \frac{\partial}{\partial z} \left(\frac{1}{\rho_i} \frac{\partial \rho_i}{\partial z} \right) = & \\
 -4\pi G (\rho_s + \rho_{HI} + \rho_h) & \quad (3) \\
 + \frac{1}{R} \frac{\partial}{\partial R} \left(R \frac{\partial \Phi_{tot}}{\partial R} \right) &
 \end{aligned}$$

where ρ_s , ρ_{HI} are the volume density of stars and HI respectively. The term on the left-hand side describes the vertical pressure, which is decided by the observed velocity dispersion of an individual component. It should be mentioned here that, for simplicity, we do not consider any variation of σ_i along z . The first term on the RHS is the gravity term, which is coupled to all the three entities, i.e., stars, HI and dark matter. The second term on the RHS is an outcome of the radial gradient of the potential, which can be estimated using the observed rotation curve of the galaxy.

$$\left(R \frac{\partial \Phi_{total}}{\partial R} \right)_{R,z} = (v_{rot}^2)_{R,z} \quad (4)$$

Assuming that the rotation curve does not change as a function of height (z), Eq. 3 can be simplified to

$$\begin{aligned}
 \langle \sigma_z^2 \rangle_i \frac{\partial}{\partial z} \left(\frac{1}{\rho_i} \frac{\partial \rho_i}{\partial z} \right) = & \\
 -4\pi G (\rho_s + \rho_{HI} + \rho_h) & \quad (5) \\
 + \frac{1}{R} \frac{\partial}{\partial R} (v_{rot}^2) &
 \end{aligned}$$

Eq. 5 represents two coupled second-order ordinary partial differential equations in $\rho_{HI}(z)$ and $\rho_s(z)$. These equations must be solved in all radii to obtain a total three-dimensional

distribution of HI. To solve Eq. 5, one needs several input parameters which are described in the next subsection.

3.1 Input parameters

There are four primary inputs to Eq. 5 which are 1) the surface densities of individual disc components which together with the dark matter halo provides the gravity (first term on the RHS) 2) The velocity dispersions of individual components, $\sigma_{z,i}$ which provides the pressure to hold the gravity in the vertical direction (first term on LHS), 3) the rotation curve which is necessary to compute the radial term (second term in RHS) and 4) the dark matter halo parameters. These input parameters are essential to solve the hydrostatic equilibrium equation.

The surface densities are one of the critical input parameters which provide gravity and primarily decide the stable equilibrium condition. We adopt the HI and the stellar surface density profiles of our sample galaxies from Oh et al. (2015). Oh et al. (2015) produced the HI surface density profiles using the robust weighted spectral cubes from the LITTLE-THINGS survey after applying tilted ring geometric parameters. This results in HI surface density profiles with a higher degree of accuracy than a simple azimuthal averaging assuming a flat disc (see Oh et al. 2015, for more details).

The stellar surface density profiles are produced by Oh et al. (2015) using *Spitzer* IRAC 3.6 μm maps from the SINGS (The Spitzer Infrared Nearby Galaxies Survey) (Kennicutt et al. 2003) and the LVL (Local Volume Legacy) survey (Dale et al. 2009) data. As compared to the optical images, the 3.6 μm maps are less affected by dust and hence, provide a more accurate estimate of the stellar mass. Not only that, but the 3.6 μm band is also insensitive to the radiation from young stellar populations, which is responsible for a large amount of radiation but constitutes only a small fraction of the total mass. The 3.6 μm images are useful

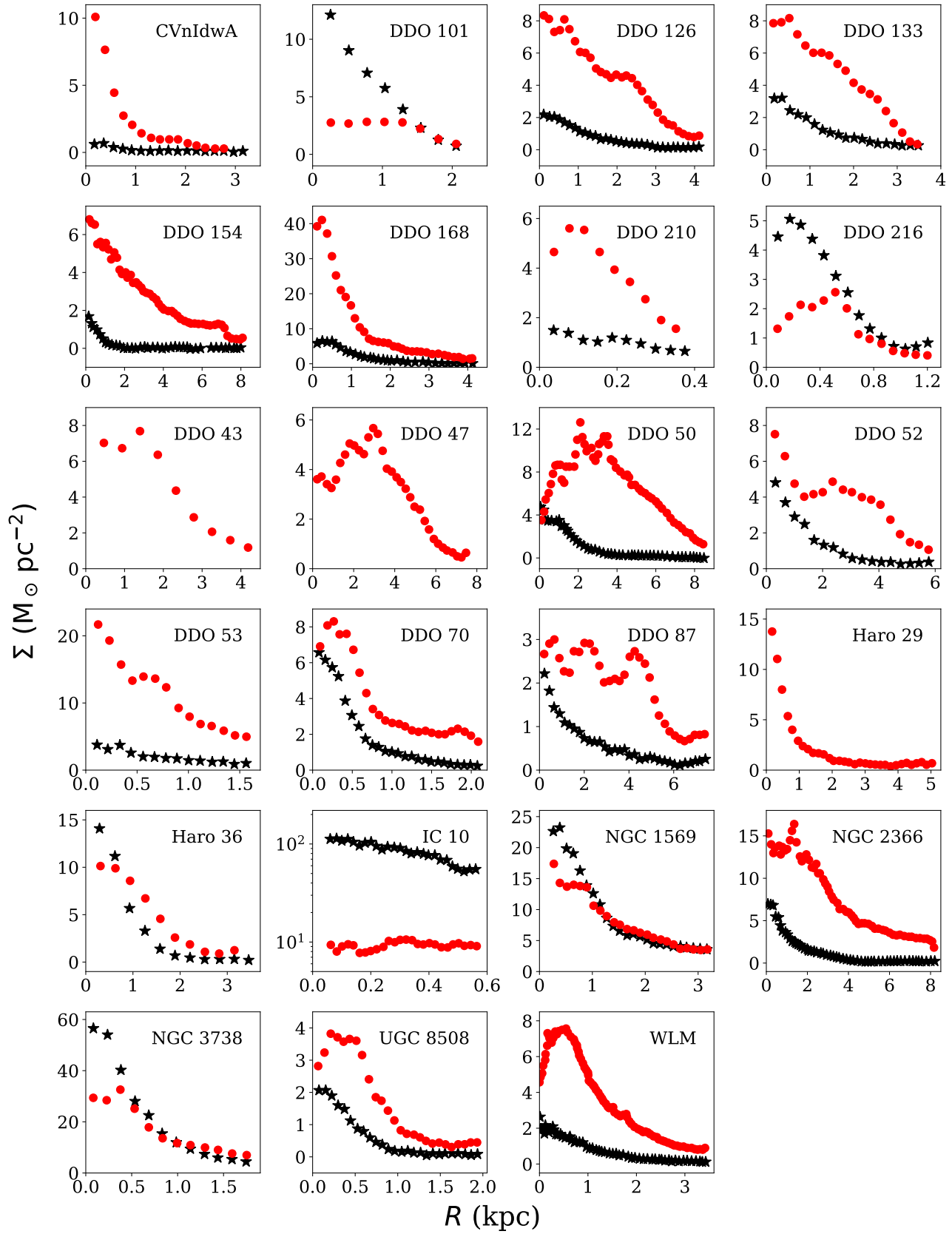


Figure 1. Surface density profiles of our sample galaxies. Individual panels represent the surface density profiles of different galaxies, as quoted in the top right corners of every panel. The black filled asterisks represent the stellar surface density profiles, whereas the red filled circles represent the atomic gas surface density profiles. The data are compiled from Oh et al. (2015).

to trace the old stellar population dominant in the late-type dwarf galaxies. Thus using $3.6 \mu\text{m}$ maps provides a robust estimate of the stellar mass surface density profile. The mass to light ratio at $3.6 \mu\text{m}$, $\Upsilon_{*}^{3.6}$ is calculated by using the empirical formula based on the stellar population synthesis model of Bruzual & Charlot (2003) and Bell & de Jong (2001). They find a typical value of $\Upsilon_{*}^{3.6} \sim 0.35$ for their sample galaxies (see Oh et al. 2011a, for more details).

Thus generated HI and stellar surface density profiles of our sample galaxies are shown in Fig. 1. As can be seen from the figure, for most of the galaxies, the HI surface density is comparable or larger than the stellar surface density. This implies that for our sample galaxies, HI dominates the surface density at almost all radii. We note here that the HI surface densities shown in Fig. 1 (and used to solve the hydrostatic equilibrium equation) is corrected by a factor 1.4 to account for Helium and metals present in the ISM. For three galaxies, i.e., DDO 43, DDO 47, and Haro 29, the stellar surface density profiles could not be produced due to the unavailability of the IRAC $3.6 \mu\text{m}$ data (see Oh et al. 2015, for more details). For these galaxies, we assume that the HI dominates the baryonic disc and solve Eq. 5 by putting $\rho_s = 0$. In fact, Oh et al. (2015) used gas surface density profiles only to produce the mass models of these three galaxies.

The vertical velocity dispersion of individual components is another input parameter that influences the vertical HI scale height directly. Unlike the surface densities, the velocity dispersion determines the vertical pressure alone and hence plays a vital role in determining the solutions of Eq. 5. Hence, a precise measurement of the same is necessary. However, it is found that while solving the hydrostatic equilibrium equation, stellar velocity dispersion does not modify the HI scale height considerably (see, e.g., Banerjee et al. 2011a). Moreover, a direct measurement of the stellar velocity dispersions in galaxies is tough using the existing observing methods. Considering these facts, we theoretically calculate the stellar velocity dispersion in our sample galaxies, assuming a prevailing hydrostatic equilibrium, as given in Leroy et al. (2008). For this calculation, the stellar disc is assumed to have an exponential vertical density distribution with a constant scale height, h_* (i.e., no flaring). The stellar scale height is then estimated using the observed flattening ratio in the optical discs of galaxies as $l_*/h_* = 7.3 \pm 2.2$ (Kregel, van der Kruit & de Grijs 2002), where l_* is the exponential disc scale length. Assuming an isothermal stellar disc in hydrostatic equilibrium and a vertical to radial velocity dispersion ratio, $\sigma_{*,z}/\sigma_{*,r} = 0.6$, the vertical stellar velocity dispersion at any radius is then computed as $\sigma_{*,z} = 1.879\sqrt{l_*\Sigma_*}$ where Σ_* is the stellar surface density (see Appendix-B.3 of Leroy et al. 2008, for more details). However, recent studies using IFU data suggest that the assumption of an isothermal stellar disc always overestimates the true velocity dispersion within the disc scale length and underestimates the same beyond the disc scale length (Mogotsi & Romeo 2018). Nonetheless, a theoretical approximation to the stellar velocity dispersion is justified here as it marginally influences the vertical HI distribution.

Unlike the stellar velocity dispersion, the HI velocity dispersion can be estimated easily using spectral line observations. Early low-resolution observations of the HI discs in external galaxies resulted in a velocity dispersion in the range between $6\text{--}13 \text{ km s}^{-1}$ (Shostak & van der Kruit 1984; van der Kruit & Shostak 1984; Kamphuis & Sancisi 1993). However, with the advent of modern-day radio telescopes, the velocity dispersions of the HI discs in nearby galaxies can be measured with high spectral and spatial resolutions. The HI spectral cubes can be used to compute a map of the second moment (MOMNT2) of the line-of-sight HI spectra. Very often, this MOMNT2 is used

as a measure of the velocity dispersion in the HI disc. For example, Tamburro et al. (2009) used the data from the THINGS survey to estimate the velocity dispersion in spiral galaxies using the MOMNT2 maps. However, though the MOMNT2 can be used as an easily available measure of the velocity dispersion, it is known to be erroneous at low SNR regions. At low SNR, MOMNT2 only samples the peak of the HI spectra, which in turn artificially reduces the HI velocity dispersion.

To avoid this SNR problem, the HI spectra within a radial bin could be stacked together to produce a stacked spectrum. This stacked spectrum has a much higher SNR than any of the individual HI spectrum in the cube and can be used to estimate the σ_{HI} , which is now free from any SNR problem. In fact, a number of studies used this stacking technique to produce and study high SNR HI spectra in galaxies. For example, Ianjamasimanana et al. (2012) stacked HI spectra of THINGS galaxies to find an HI velocity dispersion between $10\text{--}13 \text{ km s}^{-1}$. Stilp et al. (2013) has used the data from the Very Large Array ACS Nearby Galaxy Survey Treasury Program (‘VLA-ANGST’; Ott et al. (2012)) to stack the HI spectra of dwarf galaxies and found a central velocity dispersion of $\sim 5\text{--}15 \text{ km s}^{-1}$. These studies repeatedly pointed out that a stacking approach results in a better estimation of the velocity dispersion in HI discs.

Adopting a similar approach, we stack the line-of-sight HI spectra in annular rings of our sample galaxies using the HI spectral cubes from the LITTLE-THINGS survey. We use the same method for stacking, as described in de Blok et al. (2008). We first fit line-of-sight HI spectra with Gaussian Hermite Polynomials of order three to locate their centroids. After determining the centroids of all such spectra, we shift them to a common velocity. This, in turn, aligns the centers of all spectra, after which we stack them together to produce a high SNR stacked spectrum. We do this exercise for each annular ring in a galaxy, representing a particular radius. We choose the widths of the rings to be the same as the observed beamwidth. Thus obtained stacked spectra are then fitted with single Gaussian functions to estimate the σ_{HI} . We emphasize here that, a minimum SNR of 5 required to fit the HI spectra with the Gaussian Hermite polynomial (see, e.g., de Blok et al. 2008). Hence, we stack only those spectra in the cube which satisfy this minimum SNR criterion.

In Fig. 2, we show example stacked spectra for the galaxy DDO 154 at four different radii. At a radius of $\sim 1.5 \text{ kpc}$ (the top left panel), ~ 1400 spectra are found to have $\text{SNR} > 5$. The stacking of these spectra resulted in a stacked spectrum with an SNR of ~ 500 , which is much higher than the maximum SNR of any individual spectrum. At a radius of $\sim 6 \text{ kpc}$ (the bottom right panel), on the other hand, a total of ~ 200 spectra were coadded, resulting in an SNR of ~ 70 . As can be seen from the figure, single-Gaussian fits (blue dashed lines) can reasonably describe the spectra and its widths. We emphasize here that at high SNR, the MOMNT2 and the width of the fitted single-Gaussian can represent the σ_{HI} equally well. However, at a lower SNR, the MOMNT2 calculation can be affected by the presence of residual noise, especially in the wings (see, e.g., the bottom right panel of Fig. 2). In such scenarios, the sigma of the single-Gaussian fits to the spectra can better represent the widths than a simple MOMNT2. To estimate the errors in the calculated HI velocity dispersion, at each radius, we construct realizations of 100 stacked spectra by bootstrapping individual spectra from the original pool and stack them. We use these 100 stacked spectra and fit them all with single-Gaussian profiles. We then calculate the boot-strapped error as the standard deviation of the widths of these stacked spectra. We add this standard deviation to the fitting uncertainty in quadrature to calculate the total error

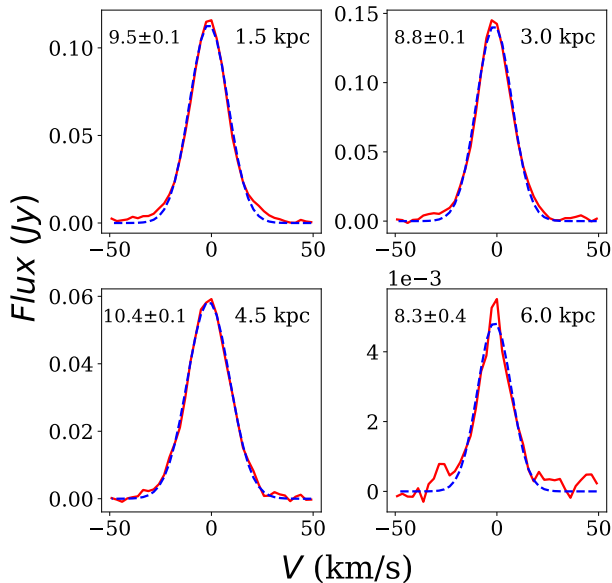


Figure 2. The stacked HI spectra and their fits to single-Gaussian profiles for DDO 154. Each panel indicates the stacked spectrum at a different radius, as quoted at the top right corner. The solid red lines indicate the stacked spectra, whereas the blue dashed lines represent a single-Gaussian fit to the same. The respective σ_{HI} are quoted in the top left corners of the individual panels in the units of km s^{-1} .

on our estimated σ_{HI} values. We note that as the spectral resolution of the HI cubes of our sample galaxies ($< 2.6 \text{ km s}^{-1}$) is much smaller than the inferred HI line-widths (see, e.g., Fig. 4), no correction is needed to account for the under-sampling of the spectra.

To compare how our derived σ_{HI} compares with other estimates, we evaluate the σ_{HI} profile in a representative galaxy DDO 154 using two other different methods. First, adopting a similar approach as Tamburro et al. (2009), we calculate the σ_{HI} by averaging the observed MOMNT2 in annular rings, as denoted by the magenta asterisks in Fig. 3. Secondly, we use the derived σ_{HI} profile in DDO 154 by Iorio et al. (2017) through a rigorous 3D tilted ring fitting using the software ^{3D}Barolo (Di Teodoro & Fraternali 2015) (black squares). As can be seen from the figure, in the inner radii, where the SNR is sufficiently high, all the three estimates of σ_{HI} match to each other within error bars. However, at larger radii, the average MOMNT2 continues to decline due to a lack of SNR, whereas, the other two estimates remain steady. Since fitting an individual spectrum with a Gaussian Hermite Polynomial requires a minimum SNR of 5, the estimation of σ_{HI} at the outermost radii is not possible. However, as the HI velocity dispersion in galaxies is found to flatten in the outer discs (see, e.g., Lewis 1984; Das et al. 2020), we assume a constant σ_{HI} in these regions which is equal to the value at the last measured point.

In Fig. 4, we plot thus obtained σ_{HI} profiles for our sample galaxies. As can be seen from the figure, there is a considerable variation in the σ_{HI} profiles as a function of radius. It is vital to capture this variation while solving the hydrostatic equilibrium equation as the vertical velocity dispersion can significantly influence the three-dimensional density distribution of the HI.

The other input to Eq. 5 is the observed rotation curve, which is necessary to compute the radial term (last term on the RHS). The rotation curve of our sample galaxies are extracted by Oh et al. (2015) using a tilted-ring model fitting to the 2D velocity field. Thus obtained rotation curves are plotted in Fig. 5. It should be noted that though the discs of dwarf galaxies show

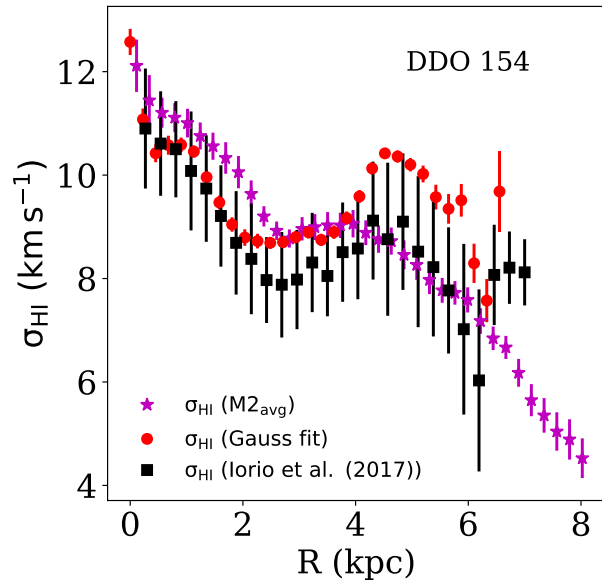


Figure 3. Comparison of the σ_{HI} profiles for DDO 154 as obtained using three different methods. The solid red circles with error bars represent the σ_{HI} as estimated by fitting single-Gaussian functions to the stacked spectra. The magenta asterisks with error bars denote σ_{HI} calculated by averaging the observed MOMNT2 within radial annuli. The solid black squares with error bars indicate the σ_{HI} derived by performing a 3D tilted ring model fitting to the HI spectral cube (Iorio et al. 2017). See the text for more details.

signs of systematic rotation (see, e.g. Begum et al. 2008), yet significant irregularities observed in their rotation curves (as can be seen from the figure). In Eq. 5, the RHS requires a first-order derivative of the rotation curve. This implies any sudden change/jump in the rotation curve (could be due to measurement errors) might lead to an unphysical value of the derivative and hence, might diverge the solutions. To avoid any such problem, we fit the rotation curves with a Brandt profile (Brandt 1960), which can be given as

$$v_{rot}(R) = \frac{V_{max}(R/R_{max})}{\left(1/3 + 2/3 \left(\frac{R}{R_{max}}\right)^n\right)^{3/2n}} \quad (6)$$

where $v_{rot}(R)$ is the rotation velocity, V_{max} is the maximum velocity attained by the rotation curve, R_{max} is the radius at which the V_{max} is observed. The index n determines how fast or slow the rotation curve reaches the V_{max} . The black dashed lines in Fig. 5, represent a Brandt-profile fit to the rotation curves of our sample galaxies.

Generally, the rotation curves, which increase as a function of radius and attains a constant flat rotation velocity, can be well described by a Brandt profile. However, for dwarf galaxies, the rotation velocity might not always reach the flat velocity (see, e.g., the rotation curve of DDO 210). In these cases, as there is no obvious V_{max} (and hence R_{max}), a Brandt profile can not produce a reasonable fit. In our sample, there are seven galaxies (CVnIdwA, DDO 210, DDO 53, DDO 70, Haro 36, NGC 1569, and UGC 8508) for which a Brandt-profile fitting could not be performed satisfactorily. For these galaxies, we find that a linear fit can describe the data reasonably well. We emphasize that we do not attempt to interpret the physical implications of the shapes of the rotation curves of our sample galaxies. We only approximate the rotation curves with a smooth function, such as a first-order derivative of the same can be computed. Hence, our

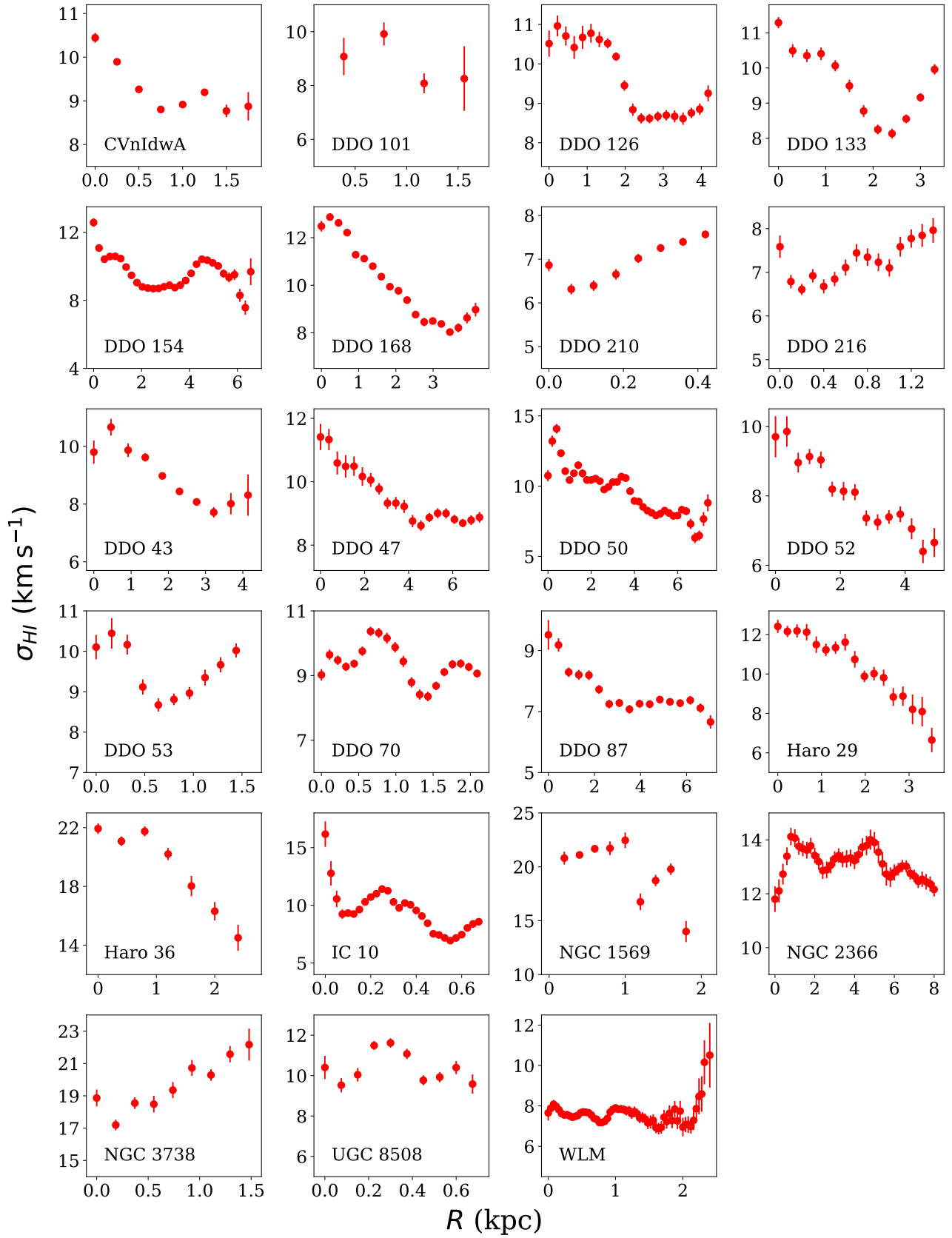


Figure 4. The σ_{HI} profiles of our sample galaxies. Each panel represents the σ_{HI} profile of an individual galaxy, as mentioned in the bottom left corner of the panel.

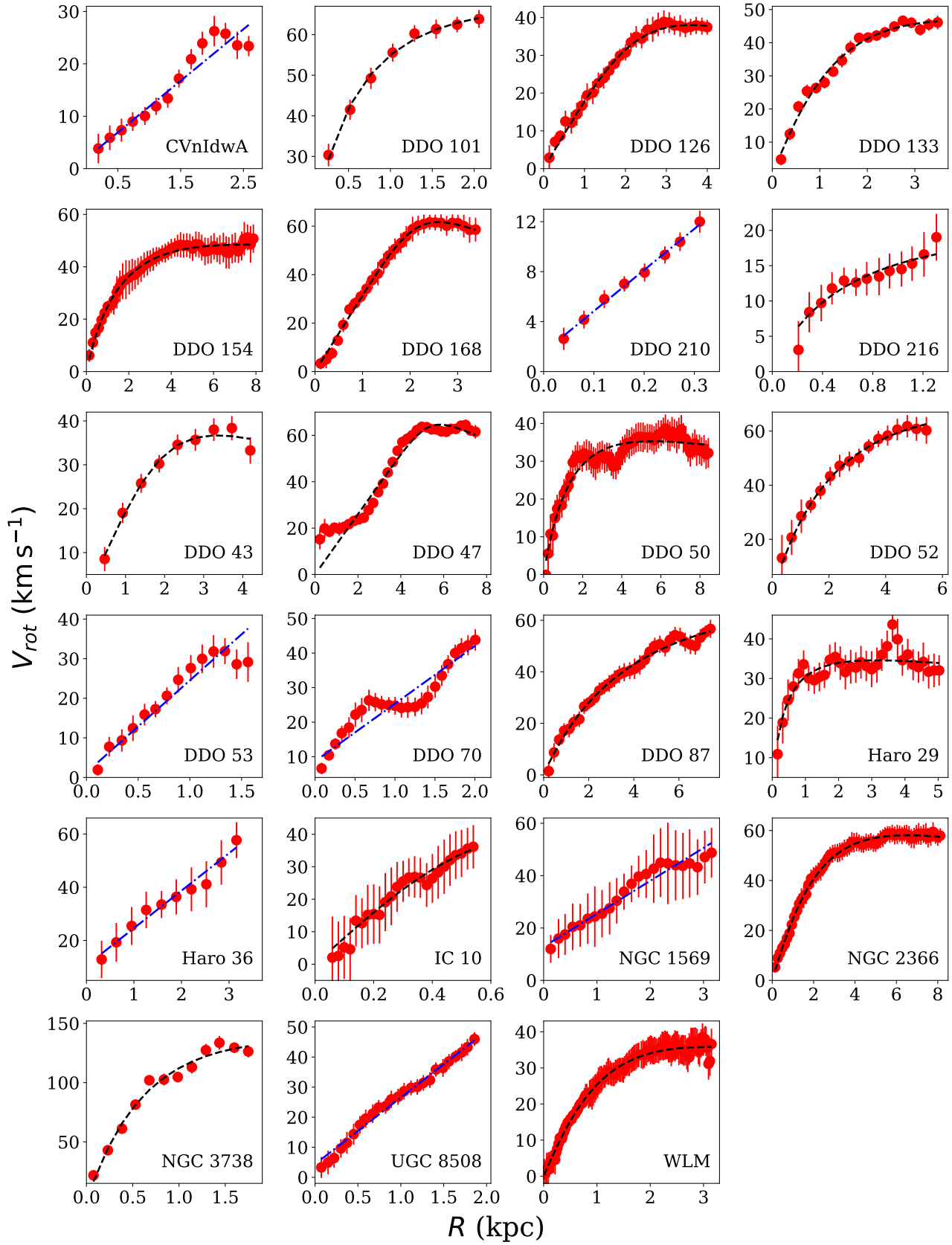


Figure 5. The rotation curves of our sample galaxies. Each panel represents the rotation curve of an individual galaxy, as mentioned in the bottom right corner of the panel. The solid red circles with error bars represent the extracted rotation velocities as a function of radius as obtained by a tilted ring fitting (Oh et al. 2015). The black dashed curves represent a Brandt-profile fit to the rotation curves, whereas the blue dashed-dotted lines represent a straight line fit to the rotation curves. See the text for more details.

Table 2. Rotation curve fit parameters

Name	Fit type (Linear/Brandt)	m ($km\ s^{-1}\ kpc^{-1}$)	c ($km\ s^{-1}$)	V_{max} ($km\ s^{-1}$)	R_{max} kpc	n
CVnIdwA	L	10±1	2.0±1.3	-	-	-
DDO 101	B	-	-	66.1±2.2	3.40±0.82	0.69±0.13
DDO 126	B	-	-	38.0±0.4	3.61±0.21	3.01±0.43
DDO 133	B	-	-	46.7±1.5	4.03±0.71	1.43±0.30
DDO 154	B	-	-	48.5±0.4	7.44±0.51	0.92±0.06
DDO 168	B	-	-	61.7±0.6	2.60±0.09	5.81±0.95
DDO 210	L	33±1	1.5±0.2	-	-	-
DDO 216	B	-	-	19.4±8.2	3.89±7.48	0.73±0.82
DDO 43	B	-	-	36.7±0.7	3.33±0.34	2.74±0.71
DDO 47	B	-	-	64.6±1.5	5.83±0.30	10.40±4.95
DDO 50	B	-	-	35.3±0.4	5.58±0.51	1.02±0.14
DDO 52	B	-	-	67.0±3.5	10.24±2.50	0.96±0.18
DDO 53	L	23±2	1.2±1.2	-	-	-
DDO 70	L	17±1	8.7±1.1	-	-	-
DDO 87	B	-	-	65.5±6.2	20.21±7.31	0.89±0.19
Haro 29	B	-	-	34.6±0.6	3.14±0.68	0.55±0.17
Haro 36	L	14±1	10.6±1.7	-	-	-
IC 10	B	-	-	43.2±18.5	1.06±1.12	2.38±2.49
NGC 1569	L	13±1	12.9±1.0	-	-	-
NGC 2366	B	-	-	58.1±0.2	6.52±0.17	1.43±0.06
NGC 3738	B	-	-	135.0±10.7	2.63±1.04	1.10±0.37
UGC 8508	L	22±1	4.4±0.7	-	-	-
WLM	B	-	-	35.8±0.3	3.09±0.13	1.51±0.08

choice to approximate some of the rotation curves by straight lines would not impact our results.

In Tab. 2, we describe the fit parameters of our rotation curves. The first column shows the name of the galaxies. Column (2) represents if the rotation curve is fitted by a Brandt profile or a straight line. Column (3) and (4) represent the slope and the intercept respectively when the rotation curve is fitted with a straight line whereas column (5), (6) and (7) show the fit parameters when the rotation curve is fitted with a Brandt profile.

The next input parameter is the dark matter halo, which provides a significant amount of gravity in the hydrostatic equilibrium equation. As described earlier, we do not consider the dark matter halo to be a live component in Eq. 5; rather, it is considered to be fixed as obtained by the mass modeling of our sample galaxies. For this purpose, we use the mass models as described in Oh et al. (2015) (Table 2). We note that in Oh et al. (2015), the mass modeling was done by considering both a pseudo-isothermal profile and an NFW profile for dark matter halo. However, a pseudo-isothermal profile found to describe the dark matter halos of nearby dwarf galaxies better than an NFW profile (Moore 1994; de Blok, McGaugh & van der Hulst 1996; de Blok & McGaugh 1997; de Blok, McGaugh & Rubin 2001; de Blok et al. 2002; Woldrake, de Blok & Walter 2003; Spekkens, Giovanelli & Haynes 2005; Kuzio de Naray et al. 2006; Kuzio de Naray, McGaugh & de Blok 2008; Oh et al. 2011b,a). For our sample galaxies, we use a pseudo-isothermal profile to describe the dark matter halos, which can be given as

$$\rho_h(R) = \frac{\rho_0}{1 + \left(\frac{R}{r_s}\right)^2} \quad (7)$$

where $\rho_h(R)$ is the density of the dark matter halo, ρ_0 is the characteristic core density, and r_s is the core radius. These two parameters completely describe a spherically symmetric pseudo-isothermal dark matter halo.

However, as the dwarf galaxies are highly dark matter dominated, the total gravity in their discs are expected to have a sub-

stantial contribution from the dark matter halo. In this sense, the structure of the dark matter halo might have a significant influence in deciding the three-dimensional distribution of HI. Hence, to investigate the same, we also solve Eq. 5 using NFW dark matter profiles in a couple of galaxies. The NFW profile can be given as (Navarro, Frenk & White 1997)

$$\rho_h(R) = \frac{\rho_0}{\frac{R}{r_s} \left(1 + \frac{R}{r_s}\right)^2} \quad (8)$$

where ρ_0 is the characteristic density and r_s the scale radius. As we adopted the dark matter halo parameters from Oh et al. (2015), we refer the readers to their Table 2 for the values of the same.

4 RESULTS AND DISCUSSION

With the above-mentioned input parameters, we solve Eq. 5 numerically. The details on how we solve the hydrostatic equilibrium equation is presented in the Appendix. We solve Eq. 5 in all our sample galaxies every 100 pc, which is equal to the median spatial resolution of the LITTLE-THINGS galaxies. We emphasize that the star formation rates at the central regions of our sample galaxies are higher than what is observed at their outer discs (see, e.g., Bigiel et al. 2010) (even though dwarf galaxies do not have a drastically high star formation rate except a few Blue Compact Dwarfs (e.g., IC 10)). This might lead to the possibility of a non-prevailing hydrostatic equilibrium at these central regions. Moreover, very often, it becomes tough to model the rotation curve at the central regions due to a lack of resolution elements and a possible presence of strong non-circular motions (see, e.g., Iorio et al. 2017). Due to these reasons, we exclude a few hundred parsecs region from the center of our sample galaxies while solving the hydrostatic equilibrium equation.

In Fig. 6, we present sample solutions of Eq. 5 for the galaxy DDO 154 at a radius of 1.5 kpc both for the HI (the magenta solid and the blue dashed lines) and the stellar (red

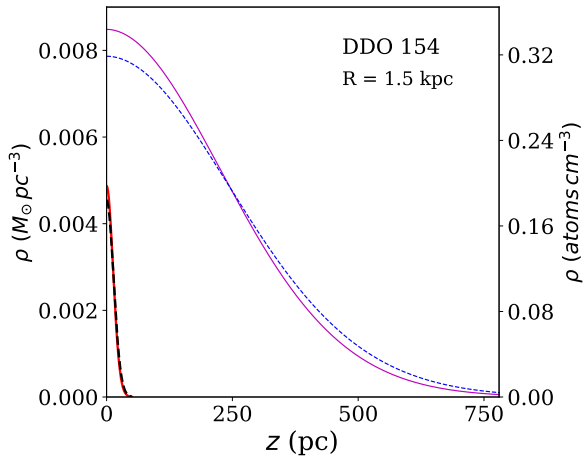


Figure 6. HI vertical density distributions, derived by solving Eq. 5 for DDO 154 at a radius of 1.5 kpc. The solid magenta and red lines represent the density distribution of the HI and the stellar discs, respectively, for an assumed ISO dark matter halo. The dashed blue and the black curves represent the solutions of the HI and stars, individually, for an NFW dark matter halo. The NFW halo found to produce lower volume densities close to the midplane (at $R = 1.5$ kpc) as compared to the ISO halo. Also, in both cases, the HI disc extends to much larger heights as compared to the stellar discs. See the text for more details.

solid and the black dashed lines) discs. We note that for a single-component isothermal disc stable under its gravity is expected to produce a solution that follows a $sech^2$ law (Spitzer 1942; Bahcall 1984b,a). However, we find that the solutions deviate from a $sech^2$ law due to the coupling between multiple disc components and the dark matter halo. In this case, the solutions are better represented by a Gaussian than a $sech^2$ function. We also find that the HI disc in DDO 154 at 1.5 kpc extends to much higher heights ($\gtrsim 750$ pc) as compared to the stellar disc. An extent of the HI disc to a height of ~ 750 pc turns out to be much higher than what is observed, for example, in the Milky Way (few hundred parsecs at $R = 10$ kpc (Kalberla et al. 2007)).

For comparison, in Fig. 6, we also plot the solutions assuming an NFW profile for the dark matter halo (the broken lines). As can be seen from the figure, there is a modest effect of the assumed dark matter halo profile on the vertical density distribution. At the central region of DDO 154 (1.5 kpc in this case), an NFW halo provides less amount of gravity close to the midplane as compared to a cored isothermal halo. Subsequently, the NFW halo results in a lower value of the HI vertical density around $z = 0$ as compared to an ISO halo. However, this does not alter the vertical scale height of the HI distribution in a significant way. We discuss this in more detail in subsequent paragraphs.

We use the solutions of Eq. 5 to estimate the HI scale heights in our sample galaxies. The HI vertical scale height at a radius can be defined as the Half Width at Half Maxima (HWHM) of the HI density distribution in the vertical direction. The scale height in galaxies traditionally being used as a measure of the thickness of the baryonic discs. In Fig. 7, we plot the HI scale heights of our sample galaxies as a function of radius. We find that the scale heights in our sample galaxies vary between a few hundred parsecs at the center to \sim a few kiloparsecs at the edge. Not only that, but a large variation in the scale heights are also observed depending on the radius and the galaxy. For example, DDO 52 (12th panel in Fig. 7) has a scale height of ~ 500 pc at the edge of its HI disc whereas, DDO 50 (11th panel) found to have a scale height of about ~ 3 kpc at its farthest radii. This variation in scale height, in fact, can

result in a distribution of shapes of the HI discs in dwarf galaxies when observed in projection (see, e.g., Roychowdhury et al. 2010, 2013).

To investigate the effect of the dark matter halo profile in deciding the HI scale height, we solve Eq. 5 for four galaxies from our sample, i.e., DDO 101, DDO 133, NGC 2366 and NGC 3738 using both the ISO and the NFW profiles. Using the density solutions, we estimate the HWHM profiles in these galaxies. In Fig. 8, we plot these HWHM profiles for both the dark matter halo profiles. We note that NGC 3738 and NGC 2366 are respectively the most and least dark matter dominated systems of our sample. The other two galaxies represent the median population. As can be seen from the figure, different dark matter distributions cause only a marginal difference in the HWHM profiles. Nevertheless, this difference increases slightly at outer radii. It can also be seen from the figure; the ISO halo systematically produces a lower HWHM in the inner galaxy and a higher HWHM in the outer radii. The turn over of the HWHM profile occurs at ~ 3 times the core radius of the ISO halo. These results indicate that a different dark matter distribution (ISO or NFW) fails to induce a detectable difference in the vertical HI density distribution. However, future sensitive observations with large facilities (e.g., the Square Kilometer Array (SKA)) might be able to distinguish the dark matter distribution in a galaxy by using its vertical HI distribution.

To further investigate the thickness of the HI discs in our sample galaxies, we estimate the axial ratios using the density solutions. The axial ratio can be defined as the ratio of two times the maximum FWHM (a measure of the disc thickness) to the diameter of the HI disc. In Fig. 9, we plot the axial ratios of our sample galaxies (solid red circles). It varies between $\sim 0.18 - 0.87$ with a median value of 0.4 (blue dashed line in the figure). This median axial ratio indicates thick HI discs in our sample galaxies. For comparison, we plot the axial ratio for the Milky Way (~ 0.13 at a radius of 40 kpc (Kalberla et al. 2007)), as shown by the black dashed-dotted line. As can be seen from the figure, the axial ratio of a typical dwarf irregular galaxy is much higher than a typical spiral galaxy. This is consistent with observations that dwarf galaxies host a much bloated/puffed HI discs (Begum et al. 2008; Roychowdhury et al. 2013; Patra et al. 2016b).

From Fig. 7, it can also be seen that the HI scale height in our sample galaxies increases as a function of radius, conferring a flaring. However, the nature of the flaring does not seem to be uniform across our sample galaxies. For example, the nature of the HI flaring in the galaxy CVnIdwA is quite different from the same in the galaxy DDO 126. To quantify this HI flaring, we fit the HI scale heights with an exponential function of the form $h_{scl} = h_0 \exp(R/l_{scl})$. Where l_{scl} represents a characteristic scale length depicting how fast or slow the scale height is rising. This could be a useful theoretical representation of the HI discs, which then can be used in numerical modeling of galaxies. The respective scale lengths of the exponential fits are quoted in the top left corners of every panel in the units of kpc. The black dashed lines in all the panels represent the exponential fit. However, it should be noted that an exponential function does not well describe all the scale heights in our sample galaxies (see, e.g., scale heights for DDO 47, DDO 53, DDO 70, etc.). For two galaxies, i.e., Haro 36 and IC 10, we do not fit an exponential function to the inferred scale height profile, since the latter does not increase monotonically as a function of radius. The large variation in the scale height profiles could arise due to the irregular nature of our sample galaxies. Unlike the large spiral galaxies where the surface densities follow a well defined exponential disc, the surface densities in dwarf galaxies are patchy and do

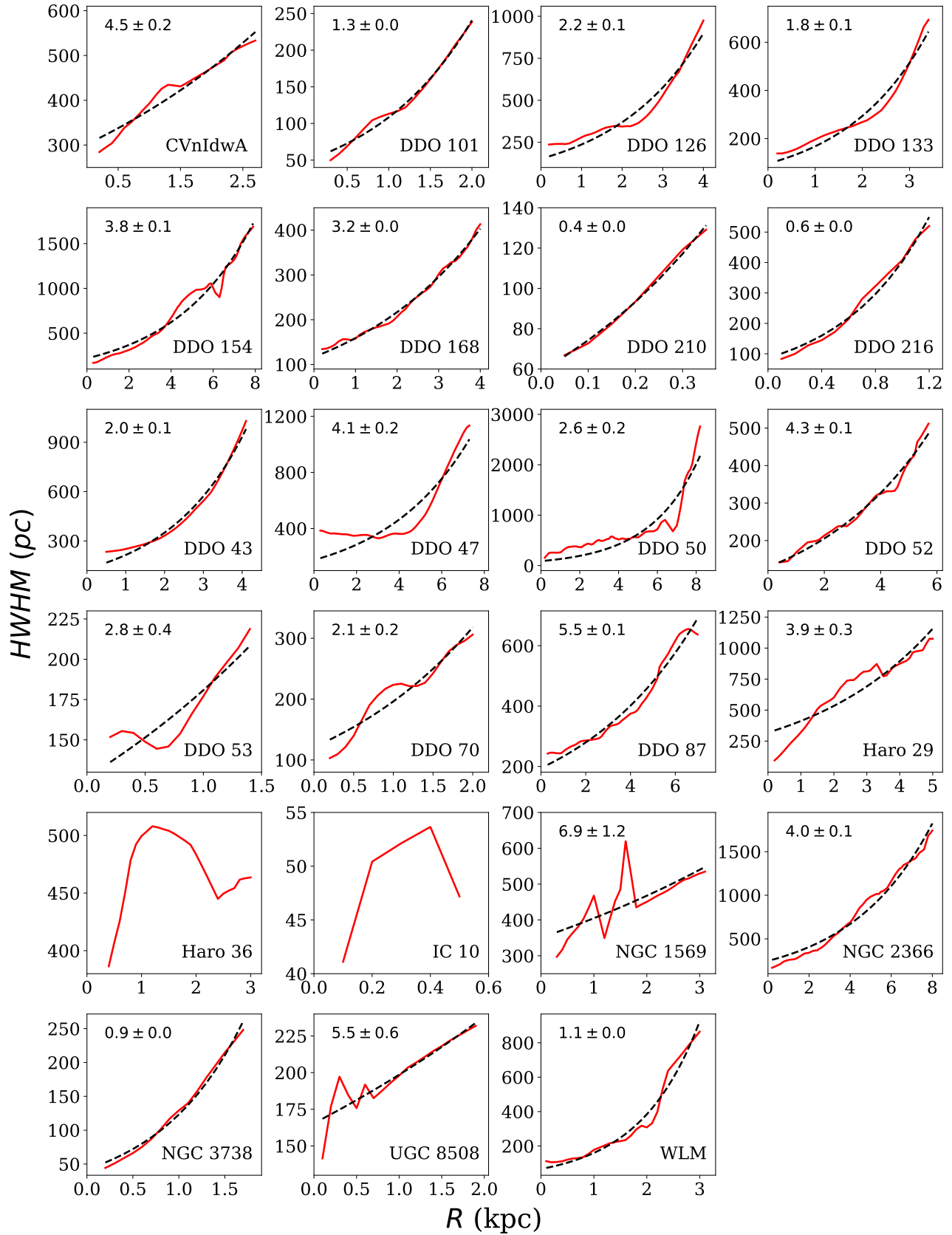


Figure 7. The HI scale height (HWHM) of our sample galaxies as a function of radius. Each panel represents the HWHM profile for different galaxies, as mentioned in the right bottom corners of the panels. The solid red lines represent the HWHM profiles, whereas the black dashed lines describe an exponential fit to it. The corresponding scale-lengths of the exponential fits are quoted in the top left corners of the respective panels.

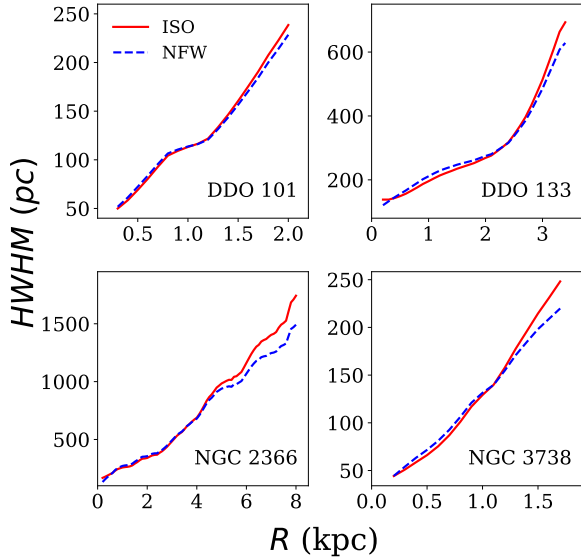


Figure 8. The effect of the assumed dark matter distribution on the HI scale height profiles. Each panel represents the scale height profile for different galaxies, as quoted at the bottom right corners. The solid red lines represent the HWHM profiles for an assumed ISO dark matter halo whereas, the blue dashed lines show the same for an NFW dark matter halo.

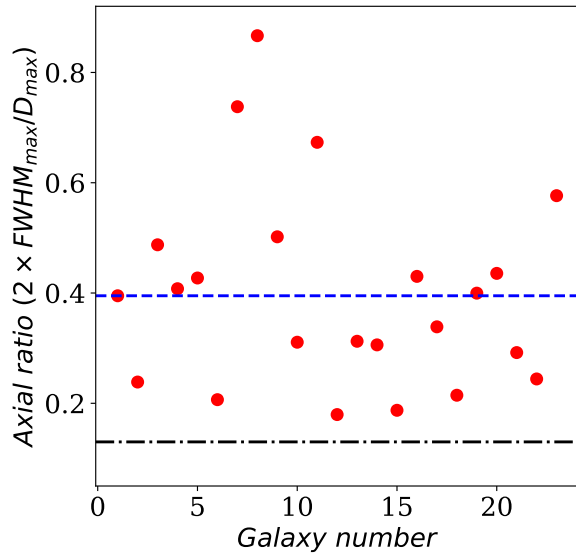


Figure 9. Axial ratios of our sample galaxies. The solid red circles are the estimated axial ratios for our sample galaxies. The blue dashed line denotes the median axial ratio of our sample galaxies, which is 0.40. The black dashed line represents the axial ratio for the Milky Way (~ 0.13) at ~ 40 kpc (Kalberla et al. 2007). This indicates that the axial ratios of dwarf galaxies are much higher than what is observed in a typical spiral galaxy. See the text for more details.

not always follow an exponential law. Moreover, many dwarf galaxies have very faint stellar discs at the central region, which in turn provide much less gravity (unlike large galaxies), leading to an extra flaring at the central region. For example, in DDO 53, the stellar surface density at the center is very low as compared to the gas surface density (see the 13th panel of Fig. 1) which results in a puffed up HI disc at these region leading to a significant deviation of the scale height from an exponential nature. However, it should be mentioned here that, the solution

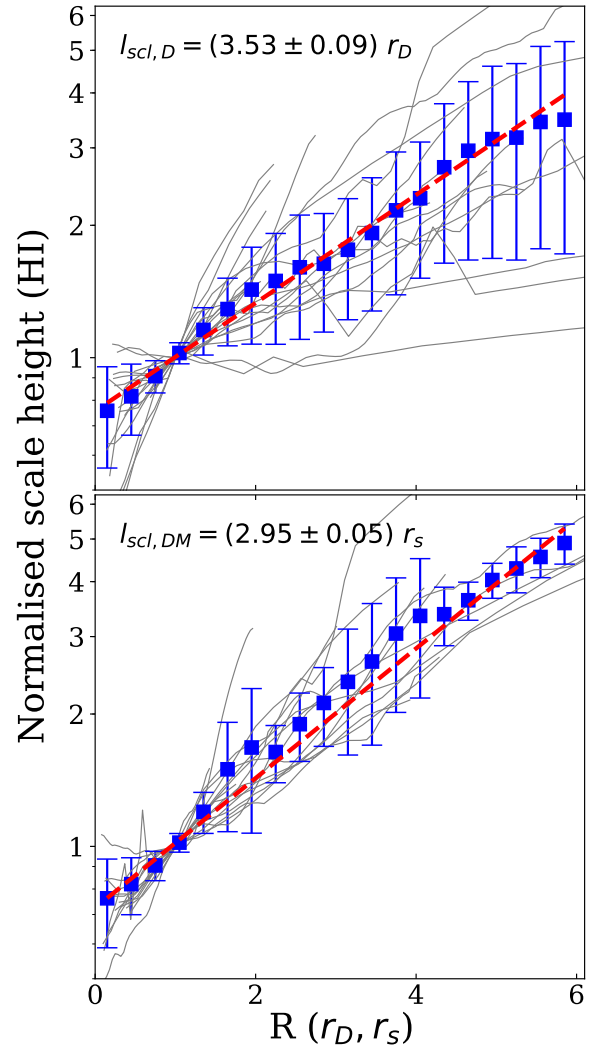


Figure 10. Normalized scale height profiles of our sample galaxies. The top panel shows the scale height profiles normalized at r_D (the optical disc scale length), whereas the bottom panel presents the HWHM profiles normalized at r_s (the core radius of the ISO dark matter halo). The grey lines in both the panels represent the normalized HI scale height profiles for individual galaxies. The blue squares with error bars denote the average normalized scale heights within a radial bin of $0.3r_D$ (top panel) or $0.3r_s$ (bottom panel). The red dashed lines represent exponential fits to the average normalized scale heights. The scale lengths of these exponential fits are quoted at the top left corners of the respective panels.

of Eq. 5 depends on many other factors as well, e.g., dark matter halo, rotation curve, HI velocity dispersion, etc. Hence, the nature of the flaring should not be attributed solely to the stellar surface density profile, though it might be a significant one. In fact, in a recent study, Bacchini et al. (2019a) estimated the HI scale height profiles in a sample of 12 nearby disc galaxies assuming a prevailing hydrostatic equilibrium. They found that the HI scale height profiles in these galaxies very often better modeled by a linear flaring than an exponential one (see their Fig. 4). However, we note that their galaxies have more massive stellar discs as compared to our sample galaxies. Consequently, we find that this leads to an increase in the amount of total gravity on the HI disc and produces less dramatic flaring. Therefore, in dwarf galaxies, a sub-dominant baryonic matter can lead to an exponential flaring of the HI disc as opposed to what is observed in large spiral galaxies.

To further investigate the universality of the flaring of the HI discs, we adopt a similar approach as used in our earlier study of molecular scale height in spiral galaxies (Patra 2018, 2019). We normalize the HI scale heights of all our sample galaxies to unity at a radius of r_D (optical disc scale length). In Fig. 10 top panel, we plot the normalized scale heights as a function of the normalized radius for all our sample galaxies except DDO 43. DDO 43 has a $r_D = 0.41$ kpc, where we did not solve the hydrostatic equation. From the figure, it can be seen that there is a significant scatter in the normalized scale height profiles as opposed to what is found for spiral galaxies (albeit for molecular gas) (see, e.g., Patra 2018, 2019). However, the dwarf galaxies are known to be dark matter dominated with a rather subdominant baryonic component. This suggests that the nature of the flaring could be regulated by the structure of the dark matter halo more than the stellar disc. Hence, in the bottom panel of Fig. 10, we plot the HI scale heights of our sample galaxies normalized to the core radius (r_s) of the ISO dark matter halo. In both the panels, we exclude Haro 36 and IC 10 as we do not choose to describe their scale height profiles by an exponential function. As can be seen from this panel, the HI scale heights normalized by the core radius show much less scatter than what is observed in the top panel. This indicates that in dwarf galaxies, the dark matter distribution mainly decides the nature of flaring in the HI discs. We further bin the normalized radius with a bin size of $0.3r_D$ or $0.3r_s$ and compute the average value of the normalized scale height in every bin (solid blue squares with error bars in both the panels). To obtain a general relation between the normalized scale height and the normalized radius, we fit these mean values with an exponential function $h_{scl} = h_0 \exp(R/l_{scl})$. We find the scale lengths as $l_{scl,D} = (3.53 \pm 0.09) r_D$ and $l_{scl,DM} = (2.95 \pm 0.05) r_s$ for our galaxies. However, despite normalizing by core radius, the HI scale height profiles still show significantly higher scatter than what is observed for spiral galaxies. This suggests that the structures of the HI discs in dwarf galaxies are not as universal as it could be for spiral galaxies.

5 CONCLUSION

We model the baryonic discs in dwarf galaxies as two-component systems consist of stars and atomic hydrogen in vertical hydrostatic equilibrium under their mutual gravity in the external force field of the dark matter halo. We subsequently set up the joint Poisson's-Boltzmann equation of hydrostatic equilibrium. We solve the hydrostatic equilibrium equation numerically using an 8th order Runge-Kutta method as implemented in the python package 'scipy'. The solutions provide a detailed three-dimensional distribution of the HI in a galaxy.

Further, the hydrostatic equilibrium equation is solved in a sample of 23 local volume dwarf galaxies from the LITTLE-THINGS survey. This is the largest sample to date for which detailed hydrostatic modeling of the HI discs is performed. The vertical velocity dispersion of the HI, σ_{HI} , is one of the crucial inputs required to solve the hydrostatic equilibrium equation. As this can influence the vertical distribution of the HI directly, a precise measurement of the same is essential. We stack the line-of-sight HI spectra from the LITTLE-THINGS survey data in radial bins to produce high SNR stacked spectra for individual galaxies. These stacked spectra are then fitted with single-Gaussian profiles to estimate the HI velocity dispersion as a function of radius. Using this σ_{HI} profile, and other input parameters, we solve the Poisson's-Boltzmann equation in our sample galaxies every 100 pc and produce a detailed three-dimensional HI density distribution in them. We further inves-

tigate the effect of the dark matter halo profile on the vertical density distribution. We find that the choice of the dark matter density distribution (ISO or NFW) does not imprint a detectable difference in the HI density distribution. Highly sensitive observations with large facilities would be essential to distinguish a dark matter halo type in a galaxy using its vertical HI distribution.

We further use the density solutions to estimate the vertical HI scale height as a function of radius. We find that the HI in dwarf galaxies flares with an increasing radius. The flaring found in our galaxies is significantly higher as compared to what is observed in typical spiral galaxies. To quantify the flaring, we fit the scale heights with an exponential function. It is found that by a large, an exponential function describes the flaring reasonably well. However though for a few galaxies, an exponential function does not provide an excellent fit. This indicates a considerable variation in the characteristic structure of the HI discs in dwarf galaxies.

We further test the universality of this HI flaring by normalizing the scale height profiles to unity at both their optical disc scale length and the core radius of the dark matter halo. Unlike spiral galaxies, which show a tight exponential behavior, dwarf galaxies are found to have a significant scatter in their normalized scale height profiles when normalized by the scale lengths of the optical disc. This scatter significantly reduces when the normalization is done using the core radius. This indicates that the structure of the dark matter halo in dwarf galaxies predominantly decides the nature of the flaring in HI discs. An exponential fit to the average normalized scale height profile (by the core radius, r_s) results in a normalized scale length $l_{scl,DM} = (2.95 \pm 0.05) r_s$.

To investigate how the thickness of the HI discs in dwarf galaxies compare to that of the spiral galaxies, we use the scale height profiles of our sample galaxies to estimate the axial ratios defined as the ratio of twice the maximum FWHM to the diameter of the HI disc. The axial ratio in our sample galaxies found to vary between $\sim 0.18 - 0.87$ with a median value of 0.40. This median axial ratio is much higher than what is observed in the Milky Way (~ 0.13). This implies that much thicker HI discs naturally occurs in dwarf irregular galaxies under vertical hydrostatic equilibrium.

6 APPENDIX

6.1 Solving the hydrostatic equation

With the input parameters mentioned in § 3.1, Eq. 5 can be solved in principle. However, this equation cannot be solved analytically even for a minimum number of disc component two. Instead, we solve this equation numerically using an Eight-order Runge-Kutta method as implemented in the python package 'scipy'.

A detailed description of the approach we adopt to solve Eq. 5 can be found in many earlier studies (see for example Narayan, Saha & Jog 2005; Banerjee & Jog 2008; Banerjee et al. 2011b; Patra et al. 2014; Patra 2018, 2019). Here we give a brief account of the scheme we use to solve the coupled hydrostatic equilibrium equation.

As Eq. 5 is a second-order partial differential equation, one needs at least two initial conditions to solve it. The two conditions are

$$(\rho_i)_{z=0} = \rho_{i,0} \quad \text{and} \quad \left(\frac{d\rho_i}{dz}\right)_{z=0} = 0 \quad (9)$$

The second condition originates by the fact that at the mid-plane, the density of both the stellar and the gas discs will be maximum, and hence, the first derivative of the same will be zero. To satisfy the first condition, we presume that the density at the mid-plane (i.e., at $z = 0$) is known ($\rho_{i,0}$). However, this mid-plane density is not a directly measurable quantity. Instead, we use the observed surface density to estimate the mid-plane density, $\rho_{i,0}$ indirectly. For any disc component (stars or gas), we start with a trial mid-plane density, $\rho_{i,t}$ and solve Eq. 5 to produce a trial density distribution $\rho_i(z)$. Now this $\rho_i(z)$ can be integrated to calculate the trial surface density, i.e., $\Sigma_i = 2 \int_0^\infty \rho_i(z) dz$. This Σ_i then can be compared with the observed surface density to update the trial mid-plane density $\rho_{i,t}$ in the next iteration. We continue this iterative process until the trial Σ_i matches the observed value with better than 1% accuracy.

Here we would like to mention that, in all previous studies, updating the trial mid-plane density was done manually. This might necessitate a large effort to solve Eq. 5 in a comprehensive number of radial points for a significant number of sample galaxies. To overcome this shortcoming, we automatize the selection of $\rho_{i,0}$ using a bisection method. For every radius, we select two trial mid-plane densities such that they produce trial surface densities which enclose the observed value. Then in every iteration using a bisection approach, we narrow down the range of the trial mid-plane density, such as it produces a trial surface density closer to the observed one. We continue this bisection process until we find a $\rho_{i,0}$, producing an observed Σ_i with better than 1% accuracy. We note that for our sample galaxies, the bisection method converges quickly within 10s of iterations without requiring any manual input.

Further, Eq. 5 represents two partial differential equations in ρ_s and ρ_{HI} , which are coupled through gravity, the first term on the RHS. Ideally, both these equations should be solved simultaneously, which is not possible. Instead, we adopt an iterative approach to include a constant density distribution (hence gravity) of one component while solving for the other one. In the first iteration, both the stars and gas are solved separately, considering no coupling. This means the density of gas made to be zero while solving for stars and vice versa. In the next iterations, one component included in the equation as a constant term while solving the other one. For example, in the first iteration, we solve for stars and gas with no coupling and produce $\rho_{s,1}(z)$ and $\rho_{HI,1}(z)$. Here the second index indicates the iteration number. In the second iteration, while solving for stars, we introduce $\rho_{HI,1}(z)$ in the first term of RHS in Eq. 5 and keep it constant. Now in the second iteration, the density distribution of the stars is produced in the presence of a gas disc, albeit the gas density distribution is not entirely correct. Similarly, we solve for gas in the presence of star and produce $\rho_{s,2}(z)$ and $\rho_{HI,2}(z)$, which are slightly better than the density distribution obtained in the first iteration. We continue this iterative method until the density distributions of the disc components converge and do not change at better than 1% level. We find that for our sample galaxies, this method quickly converges within a few iterations.

It should be emphasized here that Eq. 5 has to be solved for a large number of radial points for all our sample galaxies. As solving Eq. 5, at a radius, does not depend on the solutions at any other radius, it can be solved parallelly. We employ MPI base parallel coding to solve Eq. 5 simultaneously at multiple radii. This significantly reduces the computation time to generate the density solutions. It should be noted that a manual inspection to search for the correct trial mid-plane density, $\rho_{i,t}$ would have been restricted the implementation of parallel processing. In that sense, the bisection approach plays an indispensable role in the automation of the differential equation solver.

REFERENCES

- Bacchini C., Fraternali F., Iorio G., Pezzulli G., 2019a, *A&A*, 622, A64
 Bacchini C., Fraternali F., Pezzulli G., Marasco A., Iorio G., Nipoti C., 2019b, *A&A*, 632, A127
 Bahcall J. N., 1984a, *ApJ*, 276, 169
 Bahcall J. N., 1984b, *ApJ*, 276, 156
 Banerjee A., Jog C. J., 2007, *ApJ*, 662, 335
 Banerjee A., Jog C. J., 2008, *ApJ*, 685, 254
 Banerjee A., Jog C. J., Brinks E., Bagetakos I., 2011a, *MNRAS*, 415, 687
 Banerjee A., Jog C. J., Brinks E., Bagetakos I., 2011b, *MNRAS*, 415, 687
 Banerjee A., Matthews L. D., Jog C. J., 2010, *NewA*, 15, 89
 Begum A., Chengalur J. N., Karachentsev I. D., Sharina M. E., Kaisin S. S., 2008, *MNRAS*, 386, 1667
 Bell E. F., de Jong R. S., 2001, *ApJ*, 550, 212
 Bigiel F., Leroy A., Walter F., Blitz L., Brinks E., de Blok W. J. G., Madore B., 2010, *AJ*, 140, 1194
 Brandt J. C., 1960, *ApJ*, 131, 293
 Bruzual G., Charlot S., 2003, *MNRAS*, 344, 1000
 Dale D. A. et al., 2009, *ApJ*, 703, 517
 Das M., McGaugh S. S., Ianjamasimanana R., Schombert J., Dwarakanath K. S., 2020, *ApJ*, 889, 10
 de Blok W. J. G., McGaugh S. S., 1997, *MNRAS*, 290, 533
 de Blok W. J. G., McGaugh S. S., Rubin V. C., 2001, *AJ*, 122, 2396
 de Blok W. J. G., McGaugh S. S., van der Hulst J. M., 1996, *MNRAS*, 283, 18
 de Blok W. J. G., Walter F., Brinks E., Trachternach C., Oh S.-H., Kennicutt, Jr. R. C., 2008, *AJ*, 136, 2648
 de Blok W. J. G., Zwaan M. A., Dijkstra M., Briggs F. H., Freeman K. C., 2002, *A&A*, 382, 43
 Dekel A., Sarkar K. C., Jiang F., Bournaud F., Krumholz M. R., Ceverino D., Primack J. R., 2019, *MNRAS*, 488, 4753
 Di Teodoro E. M., Fraternali F., 2015, *MNRAS*, 451, 3021
 Ekta, Chengalur J. N., Pustilnik S. A., 2008, *MNRAS*, 391, 881
 Goldreich P., Lynden-Bell D., 1965, *MNRAS*, 130, 97
 Haehnelt M. G., Steinmetz M., Rauch M., 1998, *ApJ*, 495, 647
 Hunter D. A., 2008, in *IAU Symposium*, Vol. 255, *Low-Metallicity Star Formation: From the First Stars to Dwarf Galaxies*, Hunt L. K., Madden S. C., Schneider R., eds., pp. 226–237
 Hunter D. A. et al., 2012, *AJ*, 144, 134
 Ianjamasimanana R., de Blok W. J. G., Walter F., Heald G. H., 2012, *AJ*, 144, 96
 Iorio G., Fraternali F., Nipoti C., Di Teodoro E., Read J. I., Battaglia G., 2017, *MNRAS*, 466, 4159
 Kalberla P. M. W., Dedes L., 2008, *A&A*, 487, 951
 Kalberla P. M. W., Dedes L., Kerp J., Haud U., 2007, *A&A*, 469, 511
 Kamphuis J., Sancisi R., 1993, *A&A*, 273, L31
 Kennicutt, Jr. R. C., 1998, *ApJ*, 498, 541
 Kennicutt, Jr. R. C. et al., 2003, *PASP*, 115, 928
 Kregel M., van der Kruit P. C., de Grijs R., 2002, *MNRAS*, 334, 646
 Kuzio de Naray R., McGaugh S. S., de Blok W. J. G., 2008, *ApJ*, 676, 920
 Kuzio de Naray R., McGaugh S. S., de Blok W. J. G., Bosma A., 2006, *ApJS*, 165, 461
 Leroy A. K., Walter F., Brinks E., Bigiel F., de Blok W. J. G., Madore B., Thornley M. D., 2008, *AJ*, 136, 2782
 Lewis B. M., 1984, *ApJ*, 285, 453
 Mogotsi K. M., Romeo A. B., 2018, *ArXiv e-prints*
 Moore B., 1994, *Natur*, 370, 629

- Narayan C. A., Jog C. J., 2002a, *A&A*, 390, L35
 Narayan C. A., Jog C. J., 2002b, *A&A*, 394, 89
 Narayan C. A., Saha K., Jog C. J., 2005, *A&A*, 440, 523
 Navarro J. F., Frenk C. S., White S. D. M., 1997, *ApJ*, 490, 493
 Oh S.-H., Brook C., Governato F., Brinks E., Mayer L., de Blok
 W. J. G., Brooks A., Walter F., 2011a, *AJ*, 142, 24
 Oh S.-H., de Blok W. J. G., Brinks E., Walter F., Kennicutt, Jr.
 R. C., 2011b, *AJ*, 141, 193
 Oh S.-H. et al., 2015, *AJ*, 149, 180
 Ott J. et al., 2012, *AJ*, 144, 123
 Patra N. N., 2018, *MNRAS*, 478, 4931
 Patra N. N., 2019, *MNRAS*, 484, 81
 Patra N. N., Banerjee A., Chengalur J. N., Begum A., 2014,
MNRAS, 445, 1424
 Patra N. N., Chengalur J. N., Begum A., 2013, *MNRAS*, 429,
 1596
 Patra N. N., Chengalur J. N., Karachentsev I. D., Kaisin S. S.,
 Begum A., 2016a, *MNRAS*, 456, 2467
 Patra N. N., Chengalur J. N., Karachentsev I. D., Sharina M. E.,
 2016b, *Astrophysical Bulletin*, 71, 408
 Prochaska J. X., Wolfe A. M., 1997, *ApJ*, 487, 73
 Roychowdhury S., Chengalur J. N., Begum A., Karachentsev
 I. D., 2009, *MNRAS*, 397, 1435
 Roychowdhury S., Chengalur J. N., Begum A., Karachentsev
 I. D., 2010, *MNRAS*, 404, L60
 Roychowdhury S., Chengalur J. N., Kaisin S. S., Begum A.,
 Karachentsev I. D., 2011, *MNRAS*, 414, L55
 Roychowdhury S., Chengalur J. N., Kaisin S. S., Karachentsev
 I. D., 2014, *MNRAS*, 445, 1392
 Roychowdhury S., Chengalur J. N., Karachentsev I. D., Kaisina
 E. I., 2013, *MNRAS*, 436, L104
 Roychowdhury S., Chengalur J. N., Shi Y., 2017, *A&A*, 608,
 A24
 Schruba A. et al., 2012, *AJ*, 143, 138
 Shostak G. S., van der Kruit P. C., 1984, *A&A*, 132, 20
 Spekkens K., Giovanelli R., Haynes M. P., 2005, *AJ*, 129, 2119
 Spitzer, Jr. L., 1942, *ApJ*, 95, 329
 Stilp A. M., Dalcanton J. J., Skillman E., Warren S. R., Ott J.,
 Koribalski B., 2013, *ApJ*, 773, 88
 Tamburro D., Rix H.-W., Leroy A. K., Mac Low M.-M., Walter
 F., Kennicutt R. C., Brinks E., de Blok W. J. G., 2009, *AJ*, 137,
 4424
 Taylor C. L., Kobulnicky H. A., Skillman E. D., 1998, *AJ*, 116,
 2746
 Toomre A., 1964, *ApJ*, 139, 1217
 van der Kruit P. C., Shostak G. S., 1984, *A&A*, 134, 258
 Walter F., Brinks E., de Blok W. J. G., Bigiel F., Kennicutt, Jr.
 R. C., Thornley M. D., Leroy A., 2008, *AJ*, 136, 2563
 Weldrake D. T. F., de Blok W. J. G., Walter F., 2003, *MNRAS*,
 340, 12
 Wolfe A. M., Turnshek D. A., Smith H. E., Cohen R. D., 1986,
ApJS, 61, 249
 Wolfire M. G., McKee C. F., Hollenbach D., Tielens
 A. G. G. M., 1995, *ApJ*, 453, 673
 Zwaan M. A., van der Hulst J. M., Briggs F. H., Verheijen
 M. A. W., Ryan-Weber E. V., 2005, *MNRAS*, 364, 1467